


Combining a Crop Growth Model With CNN for Underground Natural Gas Leakage Detection Using Hyperspectral Imagery

Ying Du , Jinbao Jiang , Ziwei Liu, and Yingyang Pan

Abstract—Natural gas leakage occurs frequently due to aging pipes and other factors, but is challenging to detect. In this article, a new, robust method for nondestructive natural gas microleakage detection was proposed. It combines a crop growth model with a convolutional neural network (CNN) approach to quantitatively detect underground natural gas leakage using unmanned aerial vehicle (UAV) hyperspectral imagery. The environmental stress on wheat was used as an indicator to reflect the intensity of natural gas leakage. First, a crop growth model (simple algorithm for yield, SAFY) was used to simulate the growth of wheat, and the environmental stress factor in the model was used to construct the natural gas stress index (K_{gs}). Subsequently, CNN models were used to estimate the K_{gs} value with a hyperspectral image as the input. Finally, the CNN estimated K_{gs} was used to detect the natural gas leakage in the study area. Results showed that the SAFY model K_{gs} value could effectively identify natural gas leakage, with statistically significant differences (p -value < 0.05) among three leakage levels. Furthermore, compared to a single spectral index, K_{gs} had superior robustness throughout the wheat growth period. The CNN-1D model with InceptionV2 architecture exhibited the best accuracy in estimating K_{gs} , with a robust nRMSE of 6.9%. Overall, the combined CNN and SAFY models could accurately detect natural gas leakage, and this approach is more robust than traditional spectral index-based methods. This article provides a new method for nondestructive detecting of natural gas microleakage.

Index Terms—Convolutional neural network (CNN), hyperspectral image, natural gas microleakage, simple algorithm for yield (SAFY) model.

I. INTRODUCTION

NATURAL gas is a safe, environmentally friendly, and high-quality energy source, and occupies an important market position. Pipelines are common methods of transport and underground storage is widespread [1]. However, both are susceptible to damage from natural or human factors, and the resulting gas leakage can be hazardous and result in economic

losses [2]. Therefore, it is important to detect natural gas leakage in a timely and accurate manner.

Manual methods of underground gas leakage detection are time-consuming and struggle to detect microleakage. Although remote sensing technology is commonly used in environmental monitoring, it is difficult to directly obtain underground information by optical remote sensing due to its limited soil-penetrating ability [3]. Underground gas leakage decreases soil oxygen content, thereby inhibiting aerobic respiration in plant root cells and negatively impacting plant health [4]. Therefore, the extent of underground natural gas leakage can be monitored indirectly by examining crop growth.

Hyperspectral sensors have a powerful ability to monitor plant growth by virtue of the rich spectral information that they capture [5]–[7]. In recent years, with the rapid development of unmanned aerial vehicles (UAVs), hyperspectral images have been increasingly used to monitor plant growth. Yuan *et al.* [8] and Kanning *et al.* [9] indicated that hyperspectral imagers mounted on UAVs demonstrated an ability to estimate plant population growth parameters such as leaf area index (LAI), biomass, and chlorophyll content. Furthermore, Shivers *et al.* [10] analyzed growth indicators such as crop transpiration rates to monitor water stress, using shortwave and thermal infrared images obtained from the UAV platform. Most vegetation stresses exhibited increases in visible wavelengths and a decrease in near-infrared wavelengths [11]–[13], especially the red-edge bands that are closely related to the chlorophyll content per unit area of vegetation. For natural gas stress detection, many vegetation indexes have been developed based on these bands. For example, Smith *et al.* [14] proposed a spectra index using the 725 and 702 nm bands (D725/D702) to estimate the natural gas stress of vegetation, such as grass, winter wheat, and bean. Ran *et al.* [15] studied the characteristics of canopy spectral changes in bean, corn, and grass under natural gas leakage stress, and constructed the natural gas stress index (NGSI) to detect sites of underground natural gas storage leakage. These studies were mainly conducted by selecting key spectral bands based on a few vegetation growth parameters (e.g., chlorophyll) within a single or few growth periods. The physiological characteristics of plants change during various growth periods. A single spectral index is only effective in describing a specific plant physiological characteristic, and it is difficult to effectively describe changes in plant physiological characteristics throughout the entire

Manuscript received October 9, 2021; revised December 24, 2021 and January 29, 2022; accepted February 4, 2022. Date of publication February 10, 2022; date of current version February 24, 2022. This work was supported in part by the National Natural Science Foundation of China under Grant 41871341 and Grant 41571412 and in part by the Fundamental Research Funds for the Central Universities (2020YJSDC03). (Corresponding author: Jinbao Jiang.)

The authors are with the College of Geoscience and Surveying Engineering, China University of Mining and Technology, Beijing 100083, China (e-mail: duyings@student.cumt.edu.cn; jjb@cumt.edu.cn; liuziwei@sdau.edu.cn; cjpyynal@163.com).

Digital Object Identifier 10.1109/JSTARS.2022.3150089

growth period [16], [17]. This somewhat limits the detection of underground gas leakage based on spectral indices limited. In this context, introducing crop growth models may aid in detecting underground gas leakage, as crop growth models can provide a detailed description of the crop growth process during its entire growth period and can more accurately simulate the crop's key physiological characteristics at various growth points as compared to vegetation indices. In turn, the extent of underground gas leakage can be more accurately diagnosed. However, few studies have explored this aspect.

The combination of remote sensing data and crop growth models can effectively monitor regional-scale crop growth. Satisfactory results have been achieved in previous studies for crop growth monitoring and yield forecasting [18]. In addition, some researchers have also used crop growth models coupled with remote sensing data to simulate crop growth and stress in areas with drought and heavy metal pollution [19], [20]. These models with strong mechanics have high accuracy but are difficult to mainstream owing to their complex structures, numerous constraints, and laborious parameter optimization processes. Consequently, some studies have used several simple crop growth models with clear principles and fewer parameters to estimate crop productivity [21], [22]. The simple algorithm for yield (SAFY) estimation model proposed by Duchemin *et al.* [23] is a typical simple parametric model. This model simulates crop canopy growth in daily steps based on light energy utilization with a few easily accessible parameters. Therefore, it can be easily coupled with remote sensing data for crop growth monitoring and yield forecasting [16], [24]. In addition, some studies using the SAFY model have also considered the impacts of crop growth limitations such as water stress [25]. Overall, research has shown that the SAFY model can effectively simulate the crop growth process under varied environmental stress conditions. However, few studies have used it to monitor crop stress caused by natural gas leakage.

Most previous research on hyperspectral vegetation parameter estimation has used traditional machine learning methods, such as support vector machine (SVM) and random forest (RF) [26]–[28]. With the development of deep learning techniques, researchers have found that this data-driven approach is suitable for modeling structurally complex or high-dimensional data [29]. As a mainstream deep learning method, the convolutional neural network (CNN) has exhibited good performance in image data analysis [30], [31]. Applications of CNN for hyperspectral data are commonly aimed at image segmentation and target detection [32]–[34]. However, fewer studies have used it to retrieve quantitative land surface parameters. Barbosa *et al.* [35] modeled the response between crop yield and factors such as soil nutrients using CNN models with different architectures. When compared with traditional linear regression and machine learning methods, results showed the CNN models could better discriminate differences in the data's spatial structure and had higher accuracy in crop yield simulations. In addition, Zhang *et al.* [36] found that CNN performed better in terms of spectral feature extraction and modeling, compared with traditional methods, such as principal component analysis and wavelet transform. All of the above-mentioned studies showed that CNN

can effectively extract high-dimensional features from hyperspectral data. However, CNN does not perform well with small datasets. Therefore, coupling CNN with theoretical models such as crop growth models can improve their utility with respect to small sample sizes.

In this study, we present a new robust approach to detect underground natural gas microleakage based on hyperspectral UAV imagery. As a typical dryland crop, wheat's roots are particularly sensitive to the toxicity of anaerobic respiration [37]. Thus, we detected underground gas microleakage indirectly using the wheat's environmental stress, as simulated by the SAFY model. Instead of just using a spectral index or plant growth parameter, we constructed NGSI (K_{gs}) based on the environmental stress parameter of the SAFY model to quantitatively detect underground natural gas microleakage. In addition, three CNN models with different architectures were proposed and used to estimate K_{gs} of wheat from hyperspectral data. Finally, the most accurate model was selected to derive the natural gas stress distribution map based on hyperspectral images of the study area.

II. MATERIALS AND METHODS

A. Study Area and Experimental Design

The study area was located in Changziying Town (39°39'N, 116°34'E), Daxing District, Beijing, China. The average annual temperature of the study area is 11.8°C and the average annual precipitation is 550.3 mm, most of which occurs during summer. Two varieties of winter wheat, i.e., Jingdong 18 (V1) and Zhongmai 415 (V2), were cultivated in the study area, with a sowing date of October 10, 2017. Underground natural gas microleakage was simulated by laying underground natural gas pipelines in the study area and setting leakage points on the pipelines. The leakage points were located at a depth of 60 cm below the center point of each small test plot. For each test plot, the central and edge area was within 0.5 m and 1 m, respectively, from the leakage point. The natural gas leakage rate in the pipelines was set at three levels: 0 L (G0), 1 L (G1), and 1.5 L (G2) per minute. A total of 16 test plots were designed, the details of which are shown in Fig. 1.

B. Experimental Data

1) *Leaf Area Index (LAI)*: From the jointing stage (April 27, 2018) to the maturity stage (June 4, 2018), data collection was performed approximately every ten days for a total of five periods. LAI data were measured using the LAI-2200C Canopy Analysis System (LICOR Inc., Lincoln, Nebraska, USA). For G0 (no leakage), the LAI was only measured at the plot center. In the plots with natural gas leakage (G1, G2), the central and edge LAI was measured at 0.5 m and 1 m, respectively, from the leakage point on the central axis of each plot (see Fig. 1). A total of 24 sets of data were collected for each period.

2) *Field Hyperspectral Data*: The ground winter wheat canopy reflectance was measured using an SVC HR-1024i spectrometer (Spectra Vista Corporation, Poughkeepsie, NY, USA). The spectrometer was used to detect the full 350–2500 nm range,

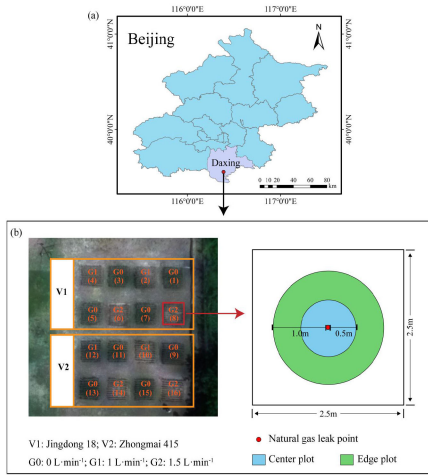


Fig. 1. Location of the study area and experimental design. (a) Location of the study area. (b) Design of treatments and images of ground-measurement field acquired from UAV mounted hyperspectral camera.

with a spectral resolution of 3.5 nm, 9.5 nm, and 6.5 nm for 350–1000 nm, 1000–1850 nm, and 1850–2500 nm, respectively. Field hyperspectral data were collected after each LAI measurement, which was performed between 10:30 A.M. and 13:30 P.M., when the weather was clear during the jointing stage (April 27, 2018) until the maturity stage (June 4, 2018). Ten measurements were made at each test plot, and the average reflectance was recorded. The collected hyperspectral data were resampled to 1-nm spacing using SVC processing software and were smoothed using the 5-point weighted average method [14] to reduce the influence of instrument noise. The NGSI was selected as a spectral index for natural gas stress on vegetation calculated as follows [15]:

$$\text{NGSI} = (R_{645} + R_{690}) / R_{800} \quad (1)$$

where R_{645} , R_{690} , and R_{800} were the reflectances at wavelengths of 645 nm, 690 nm, and 800 nm, respectively.

3) *UAV Hyperspectral Imagery*: In this study, the UHDS185 imaging spectrometer (Cubert GmbH, Ulm, Baden-Württemberg, Germany) was mounted on the DJI M600 UAV (SZ DJI Technology Co., Ltd., Sham Chun, China) to acquire hyperspectral images. Each hyperspectral image encompassed 125 wavelength bands between 450 and 950 nm. The spectral resolution was 4 nm and the image resolution was 1000×1000 pixels. At noon (10:30–13:30) on a clear day, the UAV carried a sensor and flew at an altitude of 100 m to acquire a hyperspectral image of winter wheat at the end of the filling stage (May 29, 2018) in the study area. The hyperspectral image may be affected by factors such as sensor performance and atmospheric transmission. In this study, the Cube-Pilot software (Cubert GmbH, Ulm, Baden-Württemberg, Germany) was used for image fusion preprocessing. The study area was small enough to be covered by a single view image. Therefore, only radiometric and atmospheric correction and cropping were necessary. The PIE-Hyp 6.0 software (PIESAT Information Technology Co., Ltd., Beijing, China) was used for these processes.

4) *Meteorological Data*: The meteorological reanalysis data used in this study were obtained from the European Center for Medium-Range Weather Forecasts.¹ These data mainly included daily maximum and minimum temperatures, and net surface solar radiation in the study area during the entire wheat growth period. The data were downloaded and interpolated to the same spatial resolution as the UAV hyperspectral imagery, and further processed using Python 3.7 (Python Software Foundation Inc., Portland, OR, USA) and MATLAB 2016 (Mathworks Inc., Natick, MA, USA). The downloaded maximum and minimum temperatures were used to calculate the cumulative and average daily temperatures.

C. SAFY Model Description

The SAFY model developed by Duchemin *et al.* [23] was used to simulate the wheat grown during natural gas leakage. The model simulates crop canopy growth and dry matter accumulation based on the principle of light energy utilization. The primary steps of the dry matter accumulation simulation were as follows:

- 1) calculate the daily photosynthetic effective radiation absorbed per unit area of the canopy (APAR, $\text{MJ} \cdot \text{m}^{-2} \cdot \text{d}^{-1}$) (2);
- 2) consider the effect of temperature on crop growth;
- 3) calculate the temperature limitation factor ($F_T(T_a)$) (3);
- 4) calculate the daily dry matter growth per unit area (ΔDAM , $\text{g} \cdot \text{m}^{-2} \cdot \text{d}^{-1}$) (4), (2)–(4) shown at bottom of next page.

Where ε_c is the climate efficiency factor, R_g is the total radiation, T_{\min} is the minimum temperature for crop growth ($^{\circ}\text{C}$), ELUE is the effective light energy utilization rate, k is the extinction coefficient, T_a is the average daily temperature ($^{\circ}\text{C}$), and T_{opt} is the optimal temperature for crop growth.

The model simulates crop canopy growth by estimating LAI at the leaf growth and senescence stages (Equations (5)–(8)).

$$\Delta\text{LAI}^+ = \Delta\text{DAM} \times \text{PL} \left(\sum T_a \right) \times \text{SLA} \quad (5)$$

$$\text{PL} \left(\sum T_a \right) = 1 - \text{Pl}_a \times e^{\text{Pl}_b \times \sum T_a} \quad (6)$$

$$\Delta\text{LAI}^- = \text{LAI}_{t-1} \times \left(\sum T_a - \text{STT} \right) / R_s \quad (7)$$

$$\text{LAI}_t = \text{LAI}_{t-1} + \Delta\text{LAI}^+ + \Delta\text{LAI}^- \quad (8)$$

where ΔLAI^+ is the daily increase in LAI, Pl_a , and Pl_b are the leaf allocation parameters, SLA is the specific leaf area ($\text{m}^2 \cdot \text{g}^{-1}$), the dry weight of the leaf per unit area, STT is the threshold of cumulative temperature for leaf senescence ($^{\circ}\text{C}$), and R_s is the rate of leaf senescence ($^{\circ}\text{C} \cdot \text{d}^{-1}$).

This study mainly utilized the canopy growth simulation module of the SAFY model, and the model input parameters are shown in Table I [23]. The daily radiation and average temperature were calculated as the average values from the obtained daily net surface radiation and surface temperature. The model parameters were divided into three categories. The first type

¹<http://www.ecmwf.int/>

TABLE I
MAIN INPUTS, OUTPUTS, AND PARAMETERS TO BE CORRECTED FOR THE SAFY MODEL USED TO SIMULATE THE CANOPY GROWTH OF WHEAT [23]

| | Description | Notation | Unit | Value |
|----------------|------------------------------------|------------------|---|-----------------------|
| Inputs | Daily radiation | R_g | $\text{MJ}\cdot\text{m}^{-2}\cdot\text{d}^{-1}$ | |
| | Daily average temperature | T_a | $^{\circ}\text{C}$ | |
| Parameters I | Initial dry aboveground biomass | DAM_0 | $\text{g}\cdot\text{m}^{-2}$ | 4.5 |
| | Climate efficiency | ε_c | - | 0.48 |
| | Light interception coefficient | K | - | 0.5 |
| | Minimum temperature for growth | T_{\min} | $^{\circ}\text{C}$ | 0 |
| | The optimal temperature for growth | T_{opt} | $^{\circ}\text{C}$ | 18 |
| | Maximum temperature for growth | T_{\max} | $^{\circ}\text{C}$ | 26 |
| | Specific leaf area | SLA | $\text{m}^2\cdot\text{g}^{-1}$ | 0.02 |
| Parameters II | Partition-to-leaf function 1 | Pl_a | - | 0.1-0.7 |
| | Partition-to-leaf function 2 | Pl_b | - | 10^{-5} - 10^{-2} |
| | Sum of temperature for senescence | STT | $^{\circ}\text{C}$ | 600-2000 |
| | Rate of senescence | R_s | $^{\circ}\text{C}\cdot\text{day}^{-1}$ | 1000-20000 |
| Parameters III | Date of emergence | D_0 | Day | 10 |
| | Effective light use efficiency | ELUE | $\text{G}\cdot\text{MJ}^{-1}$ | 0-2.5 |
| Outputs | Daily leaf area index | LAI | $\text{m}^2\cdot\text{m}^{-2}$ | |
| | Daily dry aboveground biomass | DAM | $\text{g}\cdot\text{m}^{-2}\cdot\text{d}^{-1}$ | |

was the crop parameters, which can be obtained based on prior knowledge and do not need to be calibrated. The second type was the phenological parameters, which are influenced by crop cultivar. The third type was environmental stress parameters, wherein ELUE is more influenced by the crop's nutritional status. Therefore, our wheat stress analysis focused on ELUE. The ELUE ratio K_{gs} ($K_{gs} = \text{ELUE}_{\text{sample}}/\text{ELUE}_{\text{healthy}}$) between nonstressed and stressed samples was calculated to represent the amount of natural gas stress, and $\text{ELUE}_{\text{healthy}}$ was the minimum ELUE value for G0 samples.

D. SAFY Model Parameters Calibration

Parameters that required calibration in the SAFY model included the cultivar-specific parameters Pl_a , Pl_b , STT , and R_s , and the environment-specific parameter ELUE. The calibration was divided into two phases. In the first phase, each of the four cultivar-specific parameters (Pl_a , Pl_b , STT , R_s) were calibrated against nonstressed plots of two cultivars (V1G0 and V2G0). Subsequently, the environment-specific parameter (ELUE) was calibrated in the second phase at the plot scale. The global optimization algorithm SCE-UA was used for SAFY model parameter calibration [38]. The algorithm is insensitive to initial

values and avoids poor parameter optimization due to a lack of prior knowledge. This optimization algorithm was run 1000 times on each wheat dataset and the final output was the median value of the 1000 runs. In this study, LAI was used as a state variable to determine the optimal parameters, by minimizing the difference between the simulated and measured value. Root-mean-square error (RMSE) was used as a cost function (9) for parameter optimization

$$\min \rightarrow \text{RMSE} = \sqrt{\frac{1}{n} \sum_{i=1}^n (\text{LAI}_{\text{measure}} - \text{LAI}_{\text{predict}})^2} \quad (9)$$

where $\text{LAI}_{\text{measure}}$ is the measured LAI, $\text{LAI}_{\text{predict}}$ is the model-predicted LAI, and n is the number of samples.

E. CNN Model Architectures

Three CNN models with different architectures were proposed and tested in this study. Each CNN architecture convolved the corresponding adjacent input frames with 1-D and 2-D filters. The input of the 1-D model was the 1-D raw spectral data of 125 bands of each pixel. For the 2-D model, spectral lines were reshaped into images for efficient feature calculation [39]. The

$$\text{APAR} = \varepsilon_c \times R_g \times (1 - e^{k \times \text{LAI}}) \quad (2)$$

$$F_T(T_a) = \begin{cases} 1 - [(T_{\text{opt}} - T_a) / (T_{\text{opt}} - T_{\min})]^2, & \text{if } T_{\min} < T_a < T_{\text{opt}} \\ 1 - [(T_a - T_{\text{opt}}) / (T_{\max} - T_{\text{opt}})]^2, & \text{if } T_{\text{opt}} < T_a < T_{\max} \\ 0, & \text{if } T_a < T_{\min} \text{ or } T_a > T_{\max} \end{cases} \quad (3)$$

$$\Delta \text{DAM} = \text{APAR} \times \text{ELUE} \times F_T(T_a) \quad (4)$$

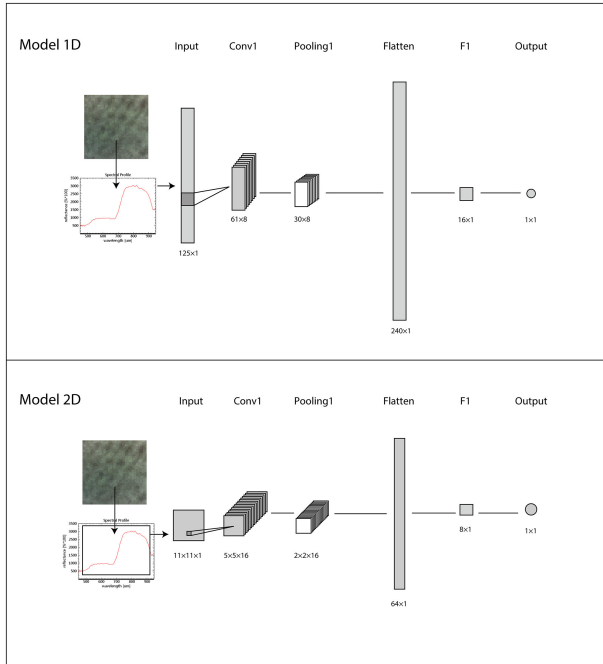


Fig. 2. CNN models with ST architecture.

input was a 2-D 11×11 tensor, which was reconstructed by rounding the first and last two bands of the spectrum of each pixel. The output of every model was the NGSI K_{gs} . The first model was a simple CNN stacking architecture (hereafter, ST) (see Fig. 2). For the 1-D model, eight 5×1 filters in the Conv1 layer transformed the 1-D spectral data into eight smaller feature maps, followed by a 2×1 maximum pooling process. Outputs were subsequently sent to the flatten layer, flattened, and then sent to the fully connected layer with 16 neurons. Finally, the outputs were sent to the output layer with a linear activation function. In the 2-D model, sixteen 3×3 filters were used in the Conv1 layer, and eight neurons were used in the fully connected layer.

The second model was based on the Inception V1 architecture [40] used by Zhang *et al.* [36] in the DeepSpectra model (hereafter V1) (see Fig. 3). It reduced computational complexity by improving the CNN's traditional convolutional layers. To further improve the CNN's learning capability and prediction accuracy, the Inception V2 architecture [40], which has a deeper model depth, was used as a basis to construct the third model in this study (hereafter V2) (see Fig. 4). For the Conv1 layer, there are filters with various sizes and numbers that are optimized in models depending on the input spectral features (see Table II). Since the dataset used in this study was small, the Early Stopping mechanism was used to prevent overfitting, which stops training if the model accuracy does not improve within 20 epochs. Furthermore, we applied BN layer, drop out, and L2 regularization strategies to further avoid overfitting. Moreover, three traditional machine learning modeling methods, partial least squares (PLS), RF, and SVM, were used in this study. The hyperparameters of the models (e.g., the number of principal

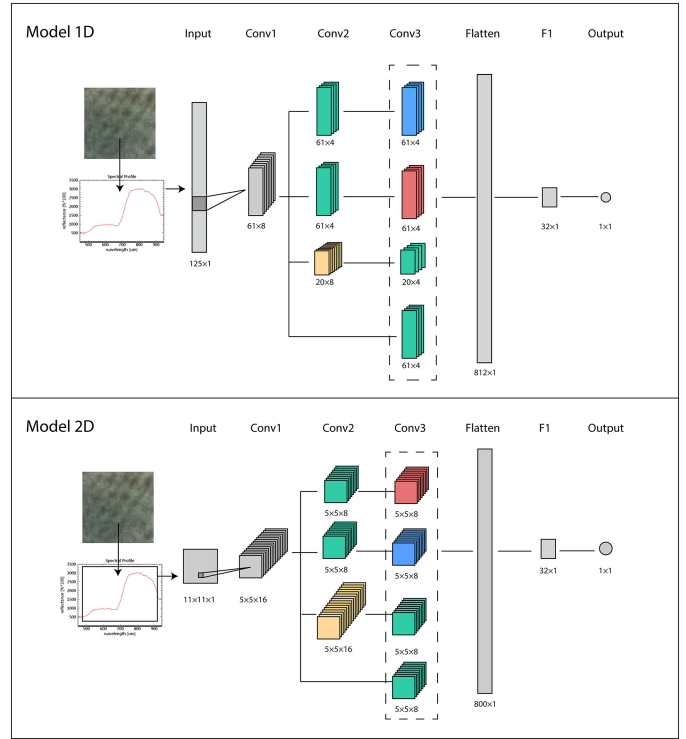


Fig. 3. CNN models with V1 architecture (blue: convolution module of size 3; green: convolution module of size 1; red: convolution module of size 5; yellow: max pooling module).

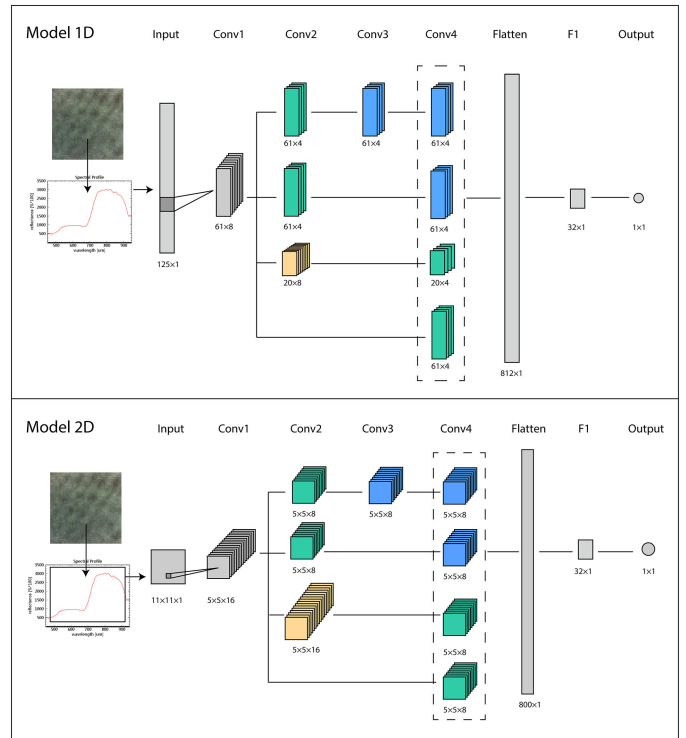


Fig. 4. CNN models with V2 architecture (blue: convolution module of size 3; green: convolution module of size 1; yellow: max pooling module).

TABLE II
MAIN HYPERPARAMETERS USED IN CNN MODELS

| Hyperparameter | CNN-1D | | | CNN-2D | | |
|---------------------|--------|-------|-------|--------|-------|-------|
| | ST | V1 | V2 | ST | V1 | V2 |
| Conv1 kernel size | 7 | 7 | 7 | 3 | 3 | 3 |
| Conv1 Stride | 2 | 2 | 2 | 2 | 2 | 2 |
| Hidden number | 16 | 32 | 32 | 8 | 32 | 32 |
| Batch size | 64 | 64 | 64 | 64 | 64 | 64 |
| Dropout rate | 0.1 | 0.2 | 0.2 | 0.1 | 0.2 | 0.2 |
| Learning rate | 0.01 | 0.01 | 0.01 | 0.01 | 0.01 | 0.01 |
| Learning rate decay | 0.001 | 0.001 | 0.001 | 0.001 | 0.001 | 0.001 |

TABLE III
CALIBRATION RESULTS FOR THE CULTIVAR-SPECIFIC PARAMETERS OF THE SAFY MODEL

| Cultivars | Pl_a | $Pl_b (10^{-4})$ | STT ($^{\circ}C$) | R_s ($^{\circ}C day^{-1}$) |
|-----------|--------|------------------|---------------------|--------------------------------|
| V1 | 0.68 | 1.73 | 1505.56 | 9998.44 |
| V2 | 0.65 | 1.87 | 1264.23 | 12572.11 |

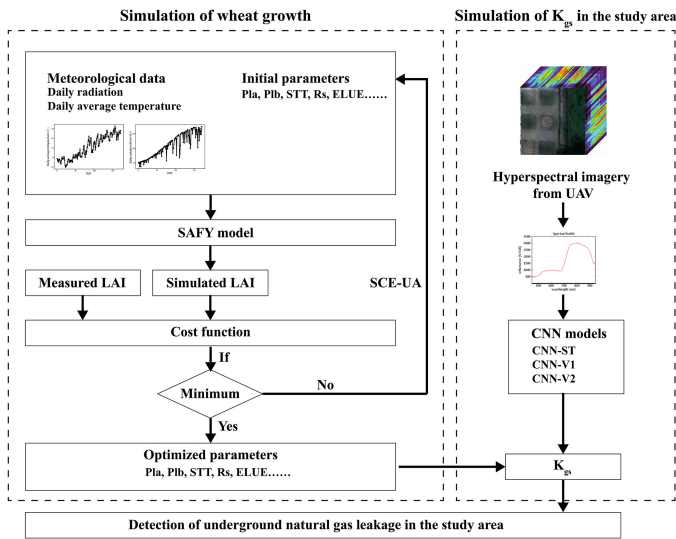


Fig. 5. Description of the detection of underground natural gas leakage in the study area.

components in the PLS model, the number of decision trees in the RF model, and the penalty factor in the SVM model) were optimized by the grid search method. Our dataset consisted of spectra of the five uniformly selected sample sites in each LAI test area. Each sample site had five tests, for a total of 600 sets of data. In total 10% of the dataset constitutes the test set. During the model training process, 20% of the remaining data constitutes the validation set, which is used for hyperparameter optimization. A flowchart illustrating underground natural gas leakage detection in the study area is shown in Fig. 5.

III. RESULTS AND ANALYSIS

A. Calibration of SAFY Model Parameters

The calibrated cultivar-specific parameters (Pl_a , Pl_b , STT, and R_s) are shown in Table III. The photosynthetic partition parameters (Pl_a , Pl_b) of the two cultivar samples had smaller differences compared to STT and R_s . Compared to the V1 cultivar, the V2 cultivar senesced earlier with a lower senescence accumulated temperature threshold (STT) and a higher senescence rate (R_s). A major reason may be that Pl_a and Pl_b had a smaller parameter adjustment range compared to STT and R_s . As shown in Fig. 6,

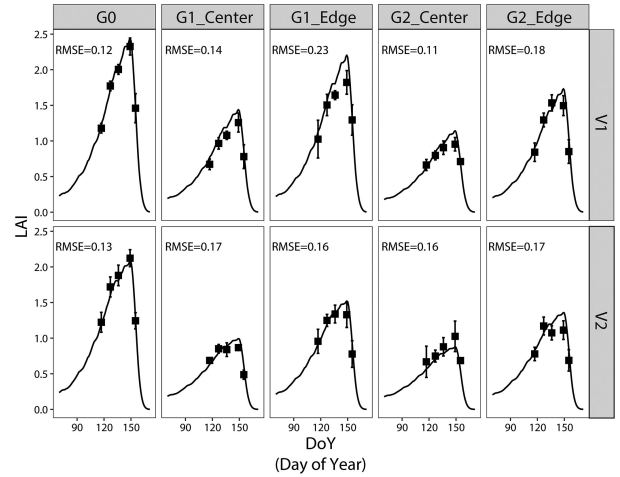


Fig. 6. LAI simulated (lines) and measured (scatters with error bars) over ten gas leakage scenarios divided according to cultivar, gas leakage rate, and sampling location.

the early LAI growth stages were similar for both cultivars, whereas the V2 cultivar had an earlier slowdown in LAI growth and a lower LAI peak. This phenomenon was more significant in the samples with greater stress. For the V1 cultivar, when the natural gas leakage rate increased from G1 (1 L·min⁻¹) to G2 (1.5 L·min⁻¹), the decrease in the LAI peak was approximately 0.2 for the central and edge area samples, respectively. The edge area samples were more sensitive to increases in gas leakage rate, whereas this phenomenon is not obvious in the V2 cultivar samples with an overall small LAI peak. This may be due to crop response to stress typically being nonlinear, and its effect on the crop has been found to increase and then decrease as stress level increases [41]. According to the simulated LAI curve peak, stress amounts (from high to low) were as follows: G2_Center, G1_Center, G2_Edge, and G1_Edge. Although the RMSE values of the various gas leakage rate samples were all satisfactory, the G0 sample exhibited the best simulated LAI curve with the least deviation from the measured LAI, especially during the late stage of wheat growth. This may be because the oxygen demand of roots varies throughout wheat growth, and the direct result of natural gas leakage on wheat is root hypoxia [4]. While the environment-specific parameter ELUE of the SAFY model was fixed, the resulting errors accumulate as the wheat grows, such that the difference between simulated and measured LAI was greater during the late growth stage.

In addition, the calibration results of the environment-specific parameter (ELUE) were consistent with the LAI simulation results. Fig. 7 shows that the ELUE values for the samples without natural gas (G0) were larger than those with natural gas

TABLE IV
DUNCAN MULTIPLE RANGE TEST FOR THE STRESS INDICES K_{gs} , NGSI, AND LAI AT DIFFERENT TREATMENTS

| Cultivars | Gas treatment | Sampling location | K_{gs} | NGSI | | | | LAI | | |
|-----------|---------------|-------------------|----------|--------|--------|--------|--------|--------|---------|-------|
| | | | | S1 | S2 | S3 | S3-UAV | S1 | S2 | S3 |
| V2 | G2 | Center | 0.55e | 0.32b | 0.87ab | 1.45a | 1.35b | 0.97c | 0.69de | 1.32c |
| | | Edge | 0.80d | 0.36ab | 0.75b | 1.29ab | 1.27b | 2.13b | 1.22b | 1.41c |
| | G1 | Center | 0.78d | 0.29b | 0.68cd | 1.06ab | 1.11b | 0.89c | 0.84cde | 1.12c |
| | | Edge | 0.87c | 0.29b | 0.56cd | 1.00b | 1.14b | 2.22ab | 1.36b | 1.15c |
| G0 | - | 1.03a | 0.30b | 0.23e | 0.43c | 0.62a | 2.56a | 2.02a | 2.12b | |
| V1 | G2 | Center | 0.66e | 0.38ab | 1.10a | 1.48a | 1.43b | 0.86c | 0.61e | 1.25c |
| | | Edge | 0.84cd | 0.60a | 1.06a | 1.41ab | 1.45b | 1.04c | 1.13bc | 1.09c |
| | G1 | Center | 0.79d | 0.26b | 0.51cd | 1.25ab | 1.31b | 0.87c | 1.02bcd | 1.31c |
| | | Edge | 0.96b | 0.28b | 0.42de | 1.00b | 1.26b | 1.18c | 1.39b | 1.27c |
| | G0 | - | 1.06a | 0.36ab | 0.26e | 0.46c | 0.69a | 1.19c | 2.12a | 2.82a |

* K_{gs} , NGSI, and LAI are the average of K_{gs} , NGSI, and LAI values for each dataset, respectively; S1, S2, and S3 are early, medium, and late growth stages, respectively; the groups marked with different letters have significant differences (p -value < 0.05) and the groups marked with the same letter do not have significant differences (p -value > 0.05).

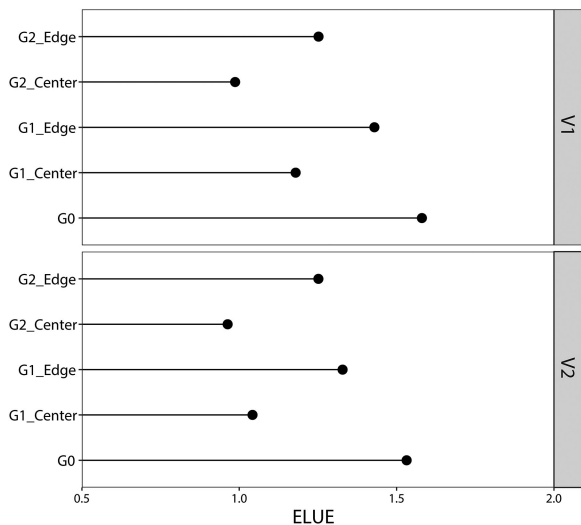


Fig. 7. ELUE simulated over ten gas leakage scenarios divided according to cultivar, gas leakage rate, and sampling location.

(G1 and G2). The ELUE values of the samples without natural gas stress were all greater than 1.5. For the stressed samples, the ELUE values of the edge samples were larger than those at the center. The ELUE values of the samples at the center of the leakage plot were approximately 1, whereas the ELUE of the edge samples leakage ranged from 1 to 1.5. There is a highly significant correlation between ELUE and natural gas leakage rate ($r = 0.94$; $p < 0.01$), as ELUE is mainly a reflection of the soil environment (e.g., moisture and nutrients), and natural gas leakage alters soil oxygen content. Overall, ELUE provides an accurate description of the impacts of natural gas leakage on wheat growth.

B. Analysis of Natural Gas Stress Index (NGSI)

The stress index K_{gs} and NGSI were calculated from the calibrated ELUE and hyperspectral data, respectively. The NGSI was calculated for three phases (S1: April 27; S2: May 13;

S3: May 29) based on ground canopy hyperspectral data, and one phase (S3: May 29) based on UAV hyperspectral imagery. In Table IV, the datasets are divided by cultivar, gas leakage rate, and sampling location. Duncan multiple range tests were performed on the calculated K_{gs} , NGSI, and measured LAI (see Table IV). For LAI alone, it was only able to distinguish between stressed and nonstressed samples of V1 cultivar and the three gas treatments of V2 cultivar in the S2 phase. The situation was similar for NGSI, which also performed best in the S2 phase. NGSI could distinguish all three gas treatments of both the V1 and V2 samples. However, the differences between sampling locations could not be distinguished for all samples with NGSI. Furthermore, comparing the ground-based NGSI with the UAV-based NGSI, it was found that the former could distinguish samples into three groups, whereas the latter could only distinguish samples into two groups during the S3 period. The UAV-based NGSI exhibited less variation between samples during the same phase, which may be due to the mixed pixels of the UAV hyperspectral imagery. The performance of NGSI on UAV hyperspectral imagery was inferior to that on ground hyperspectral imagery, which too may be caused by the mixed pixels of the UAV imagery. Furthermore, in K_{gs} , which comprehensively incorporated crop growth information, differences were observed among the three gas treatments for both the V1 and V2 samples. In addition, except for the V2 cultivar G1 gas treatment samples, samples with different sampling locations but the same gas treatment could be distinguished from each other. In comparison, K_{gs} constructed from ELUE was advantageous in detecting the extent of natural gas leakage in wheat-growing areas. A low K_{gs} value meant heavy stress on the wheat and a serious degree of gas leakage.

C. Estimation of the Degree of Natural Gas Stress

K_{gs} was used as the target feature to train the CNN-ST, CNN-V1, and CNN-V2 models with 1-D or 2-D inputs, respectively. The inputs were derived from the raw spectra of high dimensionality for each pixel on the hyperspectral image.

TABLE V
TEST ACCURACY OF MULTIPLE CNN MODELS

| Model | Architecture | nRMSE(%) | R ² |
|--------|--------------|----------|----------------|
| CNN-1D | ST | 16.5 | 0.83 |
| | V1 | 12.4 | 0.86 |
| | V2 | 6.9 | 0.90 |
| CNN-2D | ST | 9.4 | 0.82 |
| | V1 | 12.9 | 0.85 |
| | V2 | 10.8 | 0.74 |
| PLS | - | 12.6 | 0.78 |
| RF | - | 10.5 | 0.82 |
| SVM | - | 14.3 | 0.71 |

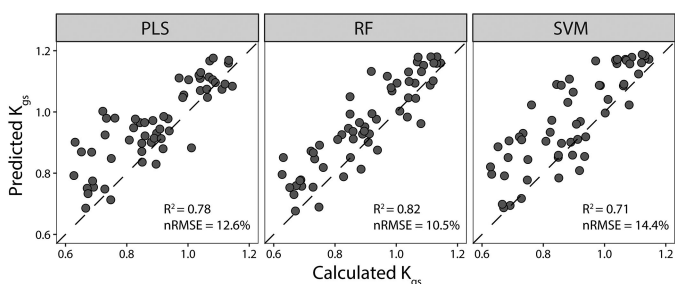


Fig. 8. Prediction results of stress index K_{gs} for machine learning models (PLS model, RF model, and SVM model).

The predicted results of the models on the test set are shown in Table V. For models with 1-D inputs, after introducing the Inception module into the simple ST architecture (nRMSE = 16.5%, $R^2 = 0.83$), the prediction accuracy of the model improved. The K_{gs} prediction accuracy of the 1D-V2 model (nRMSE = 6.9%, $R^2 = 0.90$) improved significantly compared to the 1D-V1 model (nRMSE = 12.4%, $R^2 = 0.86$). For models with 2-D inputs, compared to the ST architecture (nRMSE = 9.4%, $R^2 = 0.82$), the prediction accuracy of the 2D-V1 model (nRMSE = 12.9%, $R^2 = 0.85$) and 2D-V2 model (nRMSE = 11.5%, $R^2 = 0.74$) were not improve significantly. Furthermore, three machine learning methods (PLS, RF, and SVM) were used to predict K_{gs} based on hyperspectral data with 125 bands. The RF model exhibited higher accuracy (nRMSE = 10.5%; $R^2 = 0.82$) than the SVM (nRMSE = 14.3%; $R^2 = 0.71$) and PLS (nRMSE = 12.6%; $R^2 = 0.78$) models. The distribution of K_{gs} estimated by the machine learning models also shows that the RF model is best among the machine learning models, with predicted and calculated K_{gs} values closest to the 1:1 line (see Fig. 8). This may be because we used raw hyperspectral data and RF had a better tolerance for outliers and noise. In addition, the accuracy of the CNN models was generally higher than that of traditional machine learning models. Fig. 9 shows the distribution of K_{gs} estimated by the CNN models. The dots in the machine learning models prediction results (see Fig. 8) generally show more discrete distribution compared to dots in the CNN models prediction results (see Fig. 9). Among the CNN models, the output of CNN-1D-V2 model was closest to

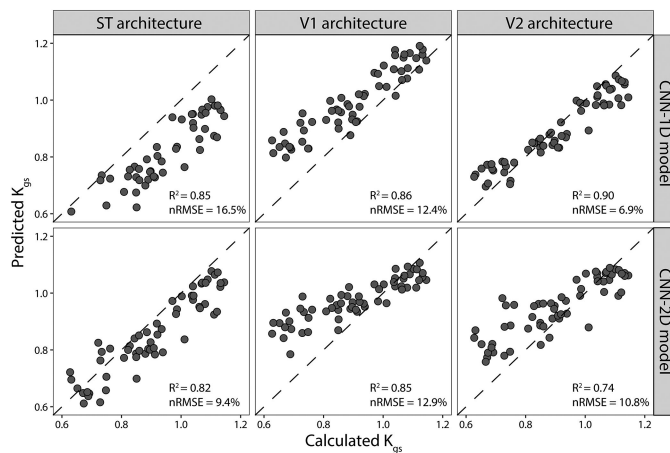


Fig. 9. Prediction results of stress index K_{gs} for CNN models (ST-CNN model, V1-CNN model, and V2-CNN model with 1-D or 2-D inputs).

the target value. Furthermore, there were overestimations of the low values in the CNN-1D-V1, CNN-2D-V1, and CNN-2D-V2 models, indicating that these models could not estimate the stress index effectively when natural gas stress occurred. Overall, the 1-D models had better learning ability for hyperspectral data features compared to the 2-D models. This may result from when hyperspectral data were used as 1-D vector inputs, the bands were continuous in the 1-D direction and the importance of the features learned by the network was high. In contrast, when the data were converted to a 2-D input, the bands' information became discontinuous, making the features learned by the network less important. In addition, based on the V1 model, the V2 model replaced one convolutional module of size 5 with two convolutional modules of size 3 and added a BN layer. It introduced more nonlinear transformations while reducing the computational effort, and further enhanced the CNN's ability to learn hyperspectral features. Therefore, the V2-CNN model with 1-D inputs was eventually selected to analyze the natural gas stress on wheat in this study.

Based on the above results, the NGSI K_{gs} was calculated for each pixel of the hyperspectral image to quantitatively describe natural gas leakage in the study area (see Fig. 10). An obvious distinction could be made between the leakage and nonleakage regions within the study area. Areas without natural gas leakage are shown in green in Fig. 10, with $K_{gs} \geq 1$. Natural gas leakage areas are shown in yellow or red (see Fig. 10), with $K_{gs} < 1$. Although the K_{gs} value did not exhibit the typical center-to-edge increasing distribution observed in some natural gas leakage plots, the simulation results in the study area were generally consistent with the test design. For V2G1 plot (labeled 12 in Fig. 10), the stress phenomenon was not obvious, possibly due to the gas leakage controller showing very small readings at the late wheat growth stage. In general, the plots with a higher gas leakage rate (G2) appeared redder and exhibited a circular feature spreading from the center to the surroundings, with $K_{gs} < 1$. For the plots with a smaller gas flow rate (G1), some green pixels with $K_{gs} \geq 1$ were evident in the image. Overall, this

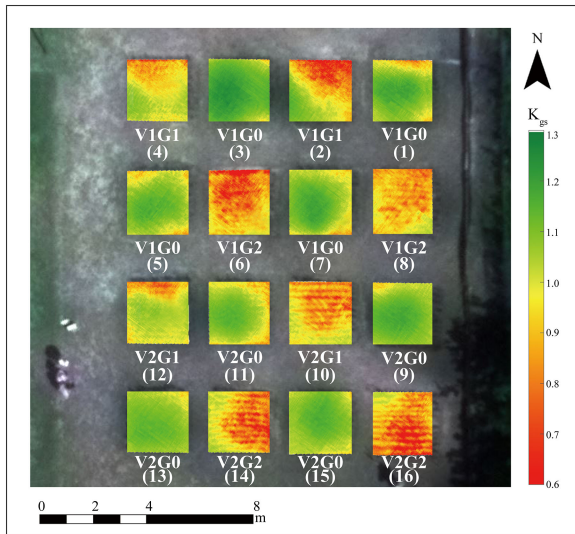


Fig. 10. Image of the extent of natural gas stress in wheat in the study area.

result was satisfactory for the detection of underground natural gas microleakage.

IV. DISCUSSION

In this study, the NGSIs K_{gs} was constructed to quantify natural gas leakage in wheat-growing areas, based on the environment-specific parameter ELUE in the SAFY model. K_{gs} was simulated by CNN models using UAV hyperspectral imagery, to identify natural gas leakage in the study area. Results were consistent with previous studies of underground oil or gas leakage in crop-growing areas [13], [42], [43]. Compared to the studies by Jiang *et al.* [11] and Noomen *et al.* [13], who used traditional empirical statistical and simple machine learning models to detect natural gas leakage, this study achieved better quantitative natural gas leakage detection results using CNN models. The main reasons for the improved results were that the SAFY model used in this study could simulate crop growth more mechanistically than empirical models alone, and the CNN model could extract features from hyperspectral data more effectively than traditional machine learning. Another difference from other studies that have relied on spectral indices of the crop canopy to detect gas leakage [14] is that we used the magnitude of environmental stress suffered by the crop as a means of detecting gas leakage. When a natural gas leakage occurs, the environmental stress on the crop is the first thing to change, followed by the plant's physiological effects that are reflected in canopy changes. In addition, plants can recover to some degree, such that the amount of stress from underground gas leakage is different from that reflected in the canopy. Therefore, there are traditional lags and inaccuracies in detecting gas leakage through canopy spectrum changes. Our method represents a potential solution to these issues.

Hyperspectral data combined with crop physiological indicators can provide better monitoring of crop stress levels. For example, He *et al.* [44] used chlorophyll content as an indicator to detect crop stress, and the spectral features from continuous

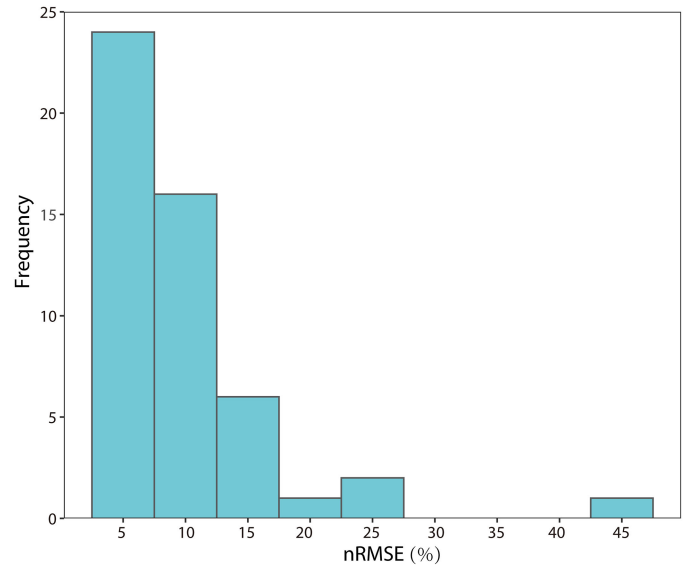


Fig. 11. Frequency distribution of nRMSE for 50 repetitions of CNN-1D model with V2 architecture.

wavelet processing of hyperspectral data were used to retrieve the characteristic physiological index. Our study differed from He's study because we considered crop growth in an integrated manner. Specifically, we obtained a more accurate calibration of the comprehensive environmental stress parameter ELUE by using the time series of LAI as an input to the SAFY model, and subsequently constructed a NGSIs (K_{gs}) based on this parameter. A comparison among K_{gs} , the spectral index, and LAI revealed that LAI and the spectral index may exhibit stability throughout crop growth. Neither the formation of crop parameters (e.g., LAI) nor the response of spectral indices to crop growth is linear. In contrast, K_{gs} demonstrated robustness throughout the period of crop growth.

It is generally believed that the predictive ability of the model is better when the training set is larger. The model output has a smaller variation coefficient with a larger sample size [45]. The model is more robust [35]. The sample size of this study was small due to the small study area. Therefore, we trained the model several times to analyze its prediction accuracy and robustness on our dataset. We retrained the CNN-1D model with V2 architecture 50 times and analyzed the prediction accuracy nRMSE of K_{gs} values. As shown in Fig. 11, the most common nRMSE values ranged from 0 to 7.5%, nearly half of the overall total. For the first two intervals (0–12.5%), the cumulative frequency was 80%, and improved to 90% for the optimal accuracy interval (0–20%). For model accuracy evaluations, it is generally accepted that the difference between predicted and measured values is small when nRMSE < 20%, indicating optimal model accuracy [46]. In conclusion, the CNN model with this architecture exhibited satisfactory accuracy and robustness. Although the sample size was small, it was reliable enough to estimate K_{gs} using hyperspectral imagery.

K_{gs} simulated by hyperspectral imagery were also effective in identifying the extent of natural gas leakage. This was consistent with previous research on the sensitivity of SAFY model

parameters to environmental stress [47], [48]. Although results were overall encouraging, the simulation results of some plots did not completely match the experimental design, possibly due to a few weed disturbances in those sample plots. The image for this study was acquired at the wheat filling stage when the wheat leaves began to wither and fall off in the field, and the canopy mainly consisted of wheat ears with low coverage. Plots with fewer natural gas leakage (G1) also exhibited better weed growth, with some weed pixels mixed in. This had a direct impact on the estimated results for the stressed plots, as some exhibited an anomalous green color near the gas leakage center. Meanwhile, some red pixels appearing at the edges of nonnatural gas plots were probably caused by the diffusion of underground gas between adjacent plots. Overall, the results support the detection of underground natural gas microleakage on a small scale. However, future studies are necessary to describe the environment-specific parameter of the SAFY model in dynamic detail and couple it with remote sensing data for regional extension applications.

V. CONCLUSION

In this study, we collected hyperspectral imagery using a UAV, then constructed NGS_I (K_{gs}) based on the SAFY model. K_{gs} was estimated using three CNN models with different architectures. Compared to a single vegetation growth parameter (LAI) and spectral index (NGSI), K_{gs} effectively reflected natural gas leakage, with good robustness observed throughout winter wheat growth. Among the CNN models, the CNN-1D model of V2 architecture could most effectively extract the feature from the original spectrum and optimally estimate K_{gs} with good robustness (nRMSE = 6.9%). These results can in turn provide theoretical and practical guidance for the quantitative and accurate detection of underground leakage.

REFERENCES

- [1] R. A. Alvarez, S. W. Pacala, J. J. Winebrake, W. L. Chameides, and S. P. Hamburg, "Greater focus needed on methane leakage from natural gas infrastructure," *Proc. Nat. Acad. Sci. USA*, vol. 109, no. 17, pp. 6435–6440, 2012.
- [2] A. R. Brandt *et al.*, "Methane leaks from North American natural gas systems," *Science*, vol. 343, no. 6172, pp. 733–735, 2014.
- [3] D. Han *et al.*, "Linking an agro-meteorological model and a water cloud model for estimating soil water content over wheat fields," *Comput. Electron. Agric.*, vol. 179, 2020, Art. no. 105833.
- [4] M. C. Drew, C.-J. He, and P. W. Morgan, "Programmed cell death and aerenchyma formation in roots," *Trends Plant Sci.*, vol. 5, no. 3, pp. 123–127, 2000.
- [5] C. Bartel *et al.*, "Modeling perennial groundcover effects on annual maize grain crop growth with the Agricultural Production Systems sIMulator," *Agronomy J.*, vol. 112, no. 3, 2019, Art. no. 1895.
- [6] Y. Cai, Y. Cai, Y. Miao, H. Wu, and D. Wang, "Hyperspectral estimation models of winter wheat chlorophyll content under elevated CO₂," *Front. Plant Sci.*, vol. 12, 2021, Art. no. 490.
- [7] G. Yang *et al.*, "Unmanned aerial vehicle remote sensing for field-based crop phenotyping: Current status and perspectives," *Front. Plant Sci.*, vol. 8, 2017, Art. no. 1111.
- [8] H. Yuan *et al.*, "Retrieving soybean leaf area index from unmanned aerial vehicle hyperspectral remote sensing: Analysis of RF, ANN, and SVM regression models," *Remote Sens.*, vol. 9, no. 4, 2017, Art. no. 309.
- [9] M. Kanning, I. Kühling, D. Trautz, and T. Jarmer, "High-resolution UAV-based hyperspectral imagery for LAI and chlorophyll estimations from wheat for yield prediction," *Remote Sens.*, vol. 10, no. 12, 2018, Art. no. 2000.
- [10] S. W. Shivers, D. A. Roberts, and J. P. McFadden, "Using paired thermal and hyperspectral aerial imagery to quantify land surface temperature variability and assess crop stress within California Orchards," *Remote Sens. Environ.*, vol. 222, pp. 215–231, 2019.
- [11] J. Jiang, W. Ran, K. Xiong, and Y. Pan, "A spectral-spatial approach for detection of single-point natural gas leakage using hyperspectral imaging," *Int. J. Greenhouse*, vol. 103, 2020, Art. no. 103181.
- [12] G. Lassalle *et al.*, "Application of PROSPECT for estimating total petroleum hydrocarbons in contaminated soils from leaf optical properties," *J. Hazardous Mater.*, vol. 377, pp. 409–417, 2019.
- [13] M. F. Noomen, A. K. Skidmore, F. D. Van der Meer, and H. H. Prins, "Continuum removed band depth analysis for detecting the effects of natural gas, methane and ethane on maize reflectance," *Remote Sens. Environ.*, vol. 105, no. 3, pp. 262–270, 2006.
- [14] K. L. Smith, M. D. Steven, and J. J. Colls, "Use of hyperspectral derivative ratios in the red-edge region to identify plant stress responses to gas leaks," *Remote Sens. Environ.*, vol. 92, no. 2, pp. 207–217, 2004.
- [15] W. Ran, J. Jiang, Y. Pan, and D. Yuan, "Spectral responses and identification of surface vegetation stressed by natural gas leakage," *Int. J. Remote Sens.*, vol. 41, no. 1, pp. 132–151, 2020.
- [16] M. Claverie *et al.*, "Maize and sunflower biomass estimation in southwest France using high spatial and temporal resolution remote sensing data," *Remote Sens. Environ.*, vol. 124, pp. 844–857, 2012.
- [17] I. Tsakmakis *et al.*, "Evaluation of AquaCrop model simulations of cotton growth under deficit irrigation with an emphasis on root growth and water extraction patterns," *Agric. Water Manage.*, vol. 213, pp. 419–432, 2019.
- [18] J. Huang *et al.*, "Evaluation of regional estimates of winter wheat yield by assimilating three remotely sensed reflectance datasets into the coupled WOFOST-PROSAIL model," *Eur. J. Agronomy*, vol. 102, pp. 1–13, 2019.
- [19] M. Liu, A. K. Skidmore, T. Wang, X. Liu, and L. Tian, "An approach for heavy metal pollution detected from spatio-temporal stability of stress in rice using satellite images," *Int. J. Appl. Earth Observ. Geoinf.*, vol. 80, pp. 230–239, 2019.
- [20] L. Leroux *et al.*, "Maize yield estimation in West Africa from crop process-induced combinations of multi-domain remote sensing indices," *Eur. J. Agronomy*, vol. 108, pp. 11–26, 2019.
- [21] X. Peng, M. Castets, C. Baron, M. J. Escorihuela, and D. L. Seen, "Assimilation of LAI derived from UAV multispectral data into the SAFY model to estimate maize yield," *Remote Sens.*, vol. 13, no. 6, 2021, Art. no. 1094.
- [22] F. Baup, W. Han, J. Ao, and Y. Wang, "Temporal evolution of corn mass production based on agro-meteorological modelling controlled by satellite optical and SAR images," *Remote Sens.*, vol. 11, no. 17, 2019, Art. no. 1978.
- [23] B. Duchemin, P. Maisongrande, G. Boulet, and I. Benhadj, "A simple algorithm for yield estimates: Evaluation for semi-arid irrigated winter wheat monitored with green leaf area index," *Environ. Model. Softw.*, vol. 23, no. 7, pp. 876–892, 2008.
- [24] M. Battude *et al.*, "Estimating maize biomass and yield over large areas using high spatial and temporal resolution Sentinel-2 like remote sensing data," *Remote Sens. Environ.*, vol. 184, pp. 668–681, 2016.
- [25] R. Hadria *et al.*, "Potentiality of optical and radar satellite data at high spatio-temporal resolutions for the monitoring of irrigated wheat crops in Morocco," *Int. J. Appl. Earth Observ. Geoinf.*, vol. 12, pp. S32–S37, 2010.
- [26] Y. Peng *et al.*, "Estimation of nitrogen content on apple tree canopy through red-edge parameters from fractional-order differential operators using hyperspectral reflectance," *J. Indian Soc. Remote Sens.*, vol. 49, pp. 1–16, 2020.
- [27] S. Luo *et al.*, "Combining hyperspectral imagery and LiDAR pseudo-waveform for predicting crop LAI, canopy height and above-ground biomass," *Ecol. Indicators*, vol. 102, pp. 801–812, 2019.
- [28] S. Luo, Y. He, Q. Li, W. Jiao, Y. Zhu, and X. Zhao, "Nondestructive estimation of potato yield using relative variables derived from multi-period LAI and hyperspectral data based on weighted growth stage," *Plant Methods*, vol. 16, no. 1, pp. 1–14, 2020.
- [29] Y. LeCun, Y. Bengio, and G. Hinton, "Deep learning," *Nature*, vol. 521, no. 7553, pp. 436–444, 2015.
- [30] O. Russakovsky *et al.*, "Imagenet large scale visual recognition challenge," *Int. J. Comput. Vis.*, vol. 115, no. 3, pp. 211–252, 2015.
- [31] R. Vaddi and P. Manoharan, "Hyperspectral image classification using CNN with spectral and spatial features integration," *Infrared Phys. Technol.*, vol. 107, 2020, Art. no. 103296.
- [32] H. Lee and H. Kwon, "Going deeper with contextual CNN for hyperspectral image classification," *IEEE Trans. Image Process.*, vol. 26, no. 10, pp. 4843–4855, Oct. 2017.

- [33] S. K. Roy, G. Krishna, S. R. Dubey, and B. B. Chaudhuri, "HybridSN: Exploring 3-D–2-D CNN feature hierarchy for hyperspectral image classification," *IEEE Geosci. Remote Sens. Lett.*, vol. 17, no. 2, pp. 277–281, Feb. 2020.
- [34] M. Zhang, W. Li, and Q. Du, "Diverse region-based CNN for hyperspectral image classification," *IEEE Trans. Image Process.*, vol. 27, no. 6, pp. 2623–2634, Jun. 2018.
- [35] A. Barbosa, W. Li, and Q. Du, "Modeling yield response to crop management using convolutional neural networks," *Comput. Electron. Agric.*, vol. 170, 2020, Art. no. 105197.
- [36] X. Zhang, T. Lin, J. Xu, X. Luo, and Y. Ying, "DeepSpectra: An end-to-end deep learning approach for quantitative spectral analysis," *Analytica Chimica Acta*, vol. 1058, pp. 48–57, 2019.
- [37] T. Fukao and J. Bailey-Serres, "Plant responses to hypoxia – Is survival a balancing act?," *Trends Plant Sci.*, vol. 9, no. 9, pp. 449–456, 2004.
- [38] Q. Duan, V. K. Gupta, and S. Sorooshian, "Shuffled complex evolution approach for effective and efficient global minimization," *J. Optim. Theory Appl.*, vol. 76, no. 3, pp. 501–521, 1993.
- [39] Z. Han and J. Gao, "Pixel-level aflatoxin detecting based on deep learning and hyperspectral imaging," *Comput. Electron. Agric.*, vol. 164, 2019, Art. no. 104888.
- [40] C. Szegedy, W. Liu, Y. Jia, P. Sermanet, and A. Rabinovich, "Going deeper with convolutions," in *Proc. IEEE Conf. Comput. Vis. Pattern Recognit.*, 2015, pp. 1–9, [Online]. Available: <https://doi.org/10.1109/CVPR.2015.7298594>
- [41] D. Raes, P. Steduto, T. C. Hsiao, and E. J. A. J. Fereres, "AquaCrop—The FAO crop model to simulate yield response to water: II Main algorithms and software description," *Agronomy J.*, vol. 101, no. 3, pp. 438–447, 2009.
- [42] J. Jiang, M. D. Steven, R. He, Y. Chen, and P. Du, "Identification of plants responding to CO₂ leakage stress using band depth and the full width at half maxima of canopy spectra," *Energy*, vol. 100, pp. 73–81, 2016.
- [43] J. Jiang, M. D. Steven, Q. Cai, R. He, H. Guo, and Y. Chen, "Detecting bean stress response to CO₂ leakage with the utilization of leaf and canopy spectral derivative ratio," *Greenhouse Gases*, vol. 4, no. 4, pp. 468–480, 2014.
- [44] R. He, H. Li, X. Qiao, and J. Jiang, "Using wavelet analysis of hyperspectral remote-sensing data to estimate canopy chlorophyll content of winter wheat under stripe rust stress," *Int. J. Remote Sens.*, vol. 39, no. 12, pp. 4059–4076, 2018.
- [45] Y. Quan *et al.*, "Spectral-spatial feature extraction based CNN for hyperspectral image classification," in *Proc. IEEE Int. Geosci. Remote Sens. Symp.*, 2020, pp. 485–488.
- [46] J. Timsina and E. Humphreys, "Performance of CERES-Rice and CERES-Wheat models in rice–wheat systems: A review," *Agric. Syst.*, vol. 90, no. 1–3, pp. 5–31, 2006.
- [47] C. Zhang *et al.*, "Evaluation of the simple algorithm for yield estimate model in winter wheat simulation under different irrigation scenarios," *Agronomy J.*, vol. 111, no. 6, pp. 2970–2980, 2019.
- [48] M. Ameline, R. Fieuzal, J. Betbeder, J. F. Berthoumieu, and F. Baup, "Estimation of corn yield by assimilating SAR and optical time series into a simplified agro-meteorological model: From diagnostic to forecast," *IEEE J. Sel. Topics Appl. Earth Observ. Remote Sens.*, vol. 11, no. 12, pp. 4747–4760, Dec. 2018.



Ying Du received the B.S. and M.S. degrees in agricultural from Yangzhou University, Yangzhou, China, in 2016 and 2019, respectively. She is currently working toward the Ph.D. degree in engineering from the College of Geosciences and Surveying Engineering, China University of Mining and Technology, Beijing, China.

Her research interests include deep learning and agricultural remote sensing.



Jinbao Jiang received the B.S. degree in engineering from the China University of Mining and Technology, Beijing, China, in 2000, and the M.S. and Ph.D. degree in engineering from Beijing Normal University, Beijing, China, in 2009.

Since 2009, he has been a Professor with China University of Mining and Technology, Beijing, China. He teaches hyperspectral remote sensing at the undergraduate and graduate levels. His main research interests include the resources and environment remote sensing, agricultural remote sensing, and deep

learning.



Ziwei Liu received the B.S. degree in engineering and the M.S. degree in agricultural from Shandong Agricultural University, Tai'an China, in 2015 and 2017, respectively. He is currently working toward the Ph.D. degree in engineering from the College of Geosciences and Surveying Engineering, China University of Mining and Technology, Beijing, China.

His research interests include deep learning, computer vision, and hyperspectral image processing.



Yingyang Pan received the B.S. degree in engineering from the Heilongjiang Institute of Technology, Harbin, China, in 2014, and the M.S. degree in engineering from Tianjin Chengjian University, Tianjin, China, in 2017. He is currently working toward the Ph.D. degree in engineering from the College of Geosciences and Surveying Engineering, China University of Mining and Technology, Beijing, China.

His research interests include deep learning, agricultural remote sensing, and hyperspectral image processing.